Automatic multi-leaf nonperiodic block-by-block pattern generation and computational analysis of historical masonry structures

M. Pereira [a], A.M. D'Altri [b,a,*], S. de Miranda [b], B. Glisic [a]

[a] *Department of Civil and Environmental Engineering, Princeton University, USA*
[b] *Department of Civil, Chemical, Environmental, and Materials Engineering, University of Bologna, Italy*

ARTICLE INFO

ABSTRACT

In this paper, an automatic block-by-block pattern generator is proposed for multi-leaf nonperiodic masonries. The outcome is then directly employed in block-based computational analysis of full-scale historical masonry structures. Given the 3D volume of the structure (obtainable also from point clouds) and the 3D block definition of a sample, both in terms of voxels, the volume of the structure is automatically filled with blocks by keeping the blocks statistics of the sample, as well as accounting for through-thickness blocks and structural details, such as lintels and edges. A meaningful benchmark is used to assess the efficiency of the filling algorithm, as well as its capability to generate statistically-consistent patterns. The benchmark is then employed in full-scale computational analyses by using an available block-based model. Various multi-leaf patterns are considered and critically compared in structural analysis, highlighting the influence of through-thickness blocks and intralayer mechanical properties on the overall structural response.

1. Introduction

Advances in numerical modelling strategies of masonry structures have been lately promoted by the need of advanced tools for the safety assessment of masonry buildings, as well as the conservation of cultural heritage (CH) structures. A significant development of numerical models for masonry has been observed in the last decades, and 4 main categories can be distinguished [1]: (i) block-based models, where the structure is considered in a block-by-block fashion; (ii) continuum models, where masonry is idealized as an equivalent homogeneous nonlinear continuum; (iii) geometry-based models, where the structure is idealized as a rigid body using limit analysis solutions; and (iv) equivalent frame models, where the structure is idealized into panel-scale structural components.

Typically, block-based models are the most accurate ones as they explicitly account for the main heterogeneity of masonry, i.e., the actual block arrangement, which basically controls the anisotropic mechanical behavior, as well as the failure mode. The main drawback of block-based models is represented by their large computational effort, which eventually limited their application mostly to panel-scale structures.

Nonetheless, latest developments on efficient models together with the recent increase of computational facilities enabled block-based

analysis of full-scale masonry structures, see for example [2,3,4,5,6,7,8,9,10]. In these examples, however, the structure had either a regular geometry/periodic masonry pattern [2,3], or an irregular geometry/nonperiodic masonry pattern that was manually created/extruded [4,5,6,7,8,9,10], i.e., a time-consuming operation that required most of the modelling-to-analysis time [5].

Furthermore, it should be underlined that the scientific community is showing particular interest about the mechanics of multi-leaf and nonperiodic masonry, see e.g. [11,12,13,14,15,16,17,18,19], where the block-by-block pattern often appears a fundamental aspect in the overall structural response.

Accordingly, a new scientific challenge is how to automatically generate detailed nonperiodic masonry arrangements (also called patterns, textures, or microstructures) for full-scale structural analysis purposes [20].

One recent way to deal with this issue considers the automatic generation of numerical models of masonry via image-based approaches [21,22,23]. Although these approaches can even account for cracked masonry [23], they are currently limited to plane structures and single-layer masonry patterns. Similarly, the automatic segmentation in blocks can be obtained directly from point clouds [24], that are typically surveyed on CH structures for documentation purposes, allowing also the
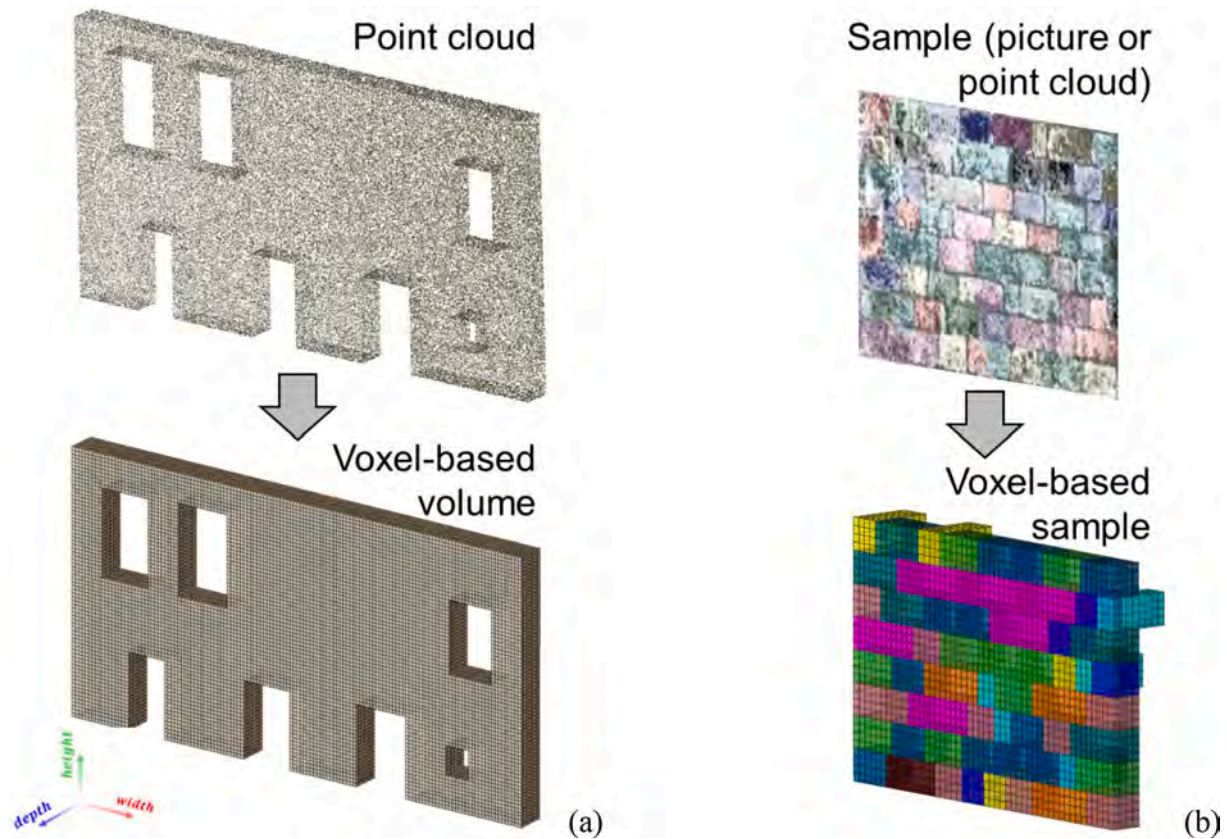

Fig. 1. Input data for the block-by-block pattern generator: (a) volume of the structure in terms of voxels (which could be generated from point clouds), and (b) 3D block definition of the sample in terms of voxels (which could be generated from pictures and/or point clouds). Picture of the masonry pattern (top right) adapted from [35].

treatment of nonplanar surfaces. However, this method has been mostly developed for defect detection rather than structural analyses purposes.

Another recent way considers automatic block-by-block pattern generators, which appears particularly appealing to obtain block-based models to be used in structural analysis. Concerning CH structures (and therefore nonperiodic pattens), a 2D typology generator for historical stone masonry has been presented in [25]. This tool has been used to correlate masonry compressive strength with the line of minimum trace in small masonry wallets. More recently, a virtual microstructure generator for 3D stone masonry walls has been presented in [26]. In this work, a multi-objective optimization packing approach, inspired by real masonry patterns, has been implemented to place the blocks in the wall. Accordingly, blocks and mortar have been explicitly considered, so that the resulting block-based numerical model consisted in a textured continuum. On the one hand, such approach can generate very accurate and realistic nonperiodic multi-leaf masonry patterns, with any kind of irregular blocks. On the other hand, the finite element (FE) meshes generated with this approach are characterized by a large number of elements and nodes, i.e., a huge computational effort. Accordingly, the 3D meshes generated in [26] could be mainly used as representative volume element (RVE) in homogenization techniques and multiscale analyses, whereas they could not yet be employed in full-scale structural analysis of masonry buildings. Also, the approach in [26] is limited to textured continuum approaches, which are typically not the most efficient block-based models [1]. Such criticalities are addressed in this research by employing a novel approach.

In this paper, a novel automatic block-by-block pattern generator is proposed for multi-leaf nonperiodic masonries. This generator requires two main input data, both in terms of voxels: (i) the 3D volume of the structure, which could be also directly obtained from point clouds by means of e.g. Cloud2FEM [27,28], and (ii) the 3D block definition in a

sample, which could be also semi-automatically obtained from images and/or point clouds [23,24], and by using machine learning [21,29]. The volume of the structure is then automatically filled with blocks by keeping the blocks statistics of the sample, as well as accounting for through-thickness blocks and structural details, e.g., lintels and edges. This outcome is then directly employed in block-based computational analysis of full-scale historical masonry structures.

A meaningful benchmark of a CH structure is used to assess the efficiency of the pattern generator, as well as the optimal target-to-sample size ratio to obtain statistically-consistent patterns. The benchmark, characterized by a 2-leaf nonperiodic masonry with horizontal bed joints, is then employed in in-plane and out-of-plane computational analyses by using a damaging block-based model previously developed by the co-authors in [3]. Various patterns, with different amounts of through-thickness blocks, are considered and critically compared in structural analysis, highlighting the influence of through-thickness blocks and intra-layer mechanical properties on the overall structural response.

This paper is organized as follows: In Section 2, the voxel-based block-by-block pattern generator is developed. In Section 3, the numerical modeling approach is presented. In Section 4, results from the numerical modeling are presented and discussed. Finally, conclusions and final remarks are given in Section 5.

2. Voxel-based block-by-block pattern generator

In this section, we develop a novel algorithm for block-by-block pattern generator based on voxels for multi-leaf nonperiodic masonries. Given a target volume $\mathscr{V} \in \mathbb{R}^{N_W \times N_H \times N_D}$ (e.g., see Fig. 1a), where N_W, N_H, N_D are, respectively, the number of voxels along the width, height, and depth of the target volume, and a texture sample $\mathscr{T} \in$
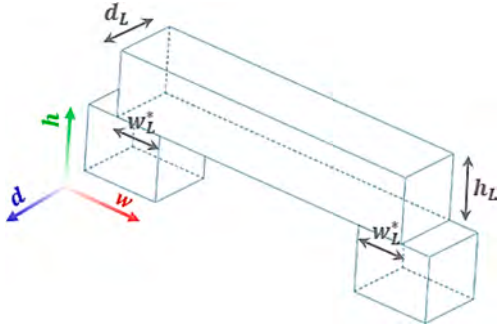
Fig. 2. Geometric parameters of automatically inserted lintels.

$\mathbb{R}^{n_w \times n_h \times n_d}$ (e.g., see Fig. 1b), where n_w, n_h, n_d are, respectively, the number of voxels along the width, height, and depth of the texture sample, the algorithm fills $\mathcal{V}$ block-by-block in a probabilistic fashion based on the proportions of each block present in $\mathcal{T}$ while seeking to avoid the alignment of blocks across vertical layers.

Typically, the external pattern is readily available (e.g., from pictures and/or point clouds [23,24,30]), while the definition of through-thickness blocks may appear more challenging and may require more in-depth investigation, e.g. through ground-penetrating radar [31,32], to increase the level of knowledge of in-situ masonry.

Ideally, we would like to generate a pattern that captures the main features of the actual structure. To this end, the sample $\mathcal{T}$ should:

(i) Include all block types that are meaningful in the reference texture.
(ii) Capture them in proportions that are representative of the reference texture.

The fulfillment of (i) and (ii) should be assessed through engineering judgment depending on the level of knowledge of the structure. Indeed, although quantitative approaches [12,33] may be followed to guarantee statistically equivalent samples in homogenization frameworks [34], the comprehensive track of the masonry pattern in CH structures is often unfeasible due to their large-scale nature, the presence of multi-leaf masonries, and budget limitations.

Furthermore, it should be underlined that the block-by-block pattern generator herein described is merely oriented to structural analysis with block-based models. In this regard, the mechanical response of samples (also called test windows or RVEs) in nonperiodic masonry has been found not to vary significantly by considering different samples extracted in distinct locations of the structure, see e.g., [35,36]. Accordingly, the fulfillment of (i) and (ii) can be considered to be satisfied in a weak way when dealing with structural analysis. Finally, it should be pointed out that if the CH structure shows different patterns in different structural portions, the algorithm herein described can be used by adopting different samples for different portions to be filled.

2.1. Filling algorithm

Certain regions of $\mathcal{V}$ may be prefilled or be non-fillable regions (e.g., openings as shown in Fig. 1a). However, to facilitate understanding of the procedure, consider first $\mathcal{V}$ without any prefilled elements or non-fillable regions. In the sample texture $\mathcal{T}$, each block type (e.g., different colors in Fig. 1b) is enumerated. Let $\mathcal{B} = \{1, \cdots, N_B\}$ be the set of all block types, where N_B is the number of block types. Let A_i denote the total area of the first leaf of $\mathcal{T}$ occupied by blocks of type i (in case, this could be readily adapted to consider the volume $\mathcal{V}_i$ of each block type instead of A_i).

Then, starting from the bottom layer of the first leaf, blocks are sampled according to the probability mass function (pmf):

$$p[\mathcal{B}](i) = \frac{A_i}{\sum_{j \in \mathcal{B}} A_j}, \ i \in \mathcal{B}, \tag{1}$$

i.e., blocks are randomly inserted following the proportions of the sample texture $\mathcal{T}$. This process occurs block-by-block, with the start position of the next block at the end of the previous block until the current horizontal layer is filled. Then, the process is repeated for the layers above. Further, one would like to avoid aligned block edges along the vertical direction. Thus, when filling a layer, the algorithm checks for the locations of vertical block edges on the layer below and determines the set $\mathcal{B}_c \subseteq \mathcal{B}$ of block types that are suitable to be inserted without alignment. We designate this requirement as constraint $\mathcal{C}_e$. Then, the generative process is governed by the pmf:

$$p[\mathcal{B}_c](i) = \frac{A_i}{\sum_{j \in \mathcal{B}_c} A_j}, \ i \in \mathcal{B}_c. \tag{2}$$

When $\mathcal{B}_c$ is empty, the generative process falls back to that of Eq. (1), so some alignment occurs in the process, which is not completely
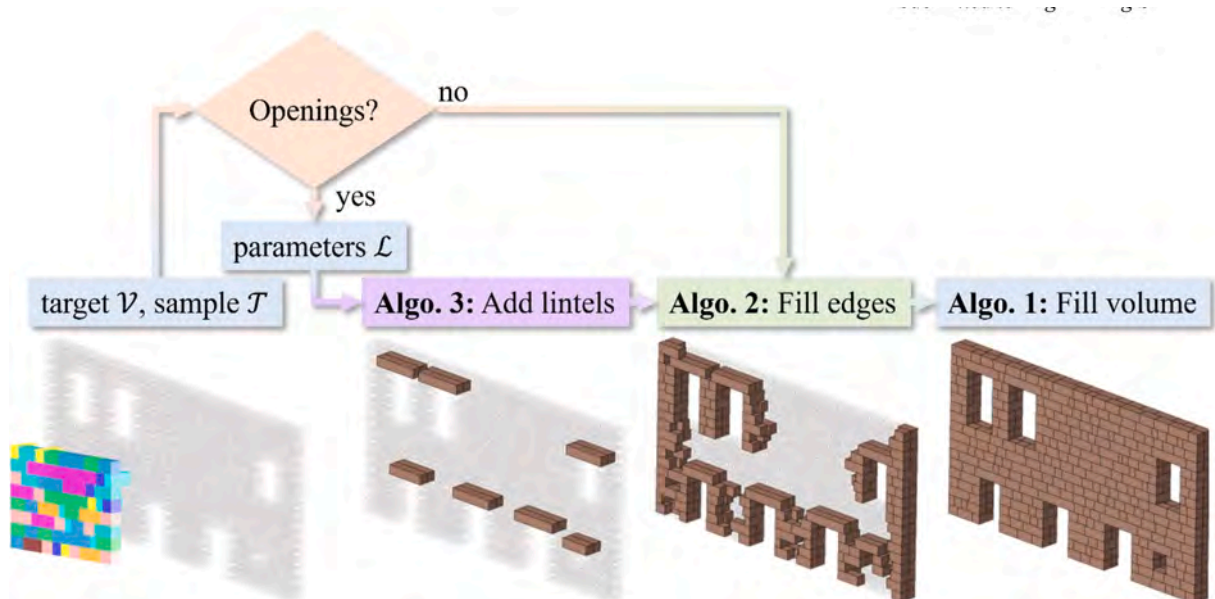

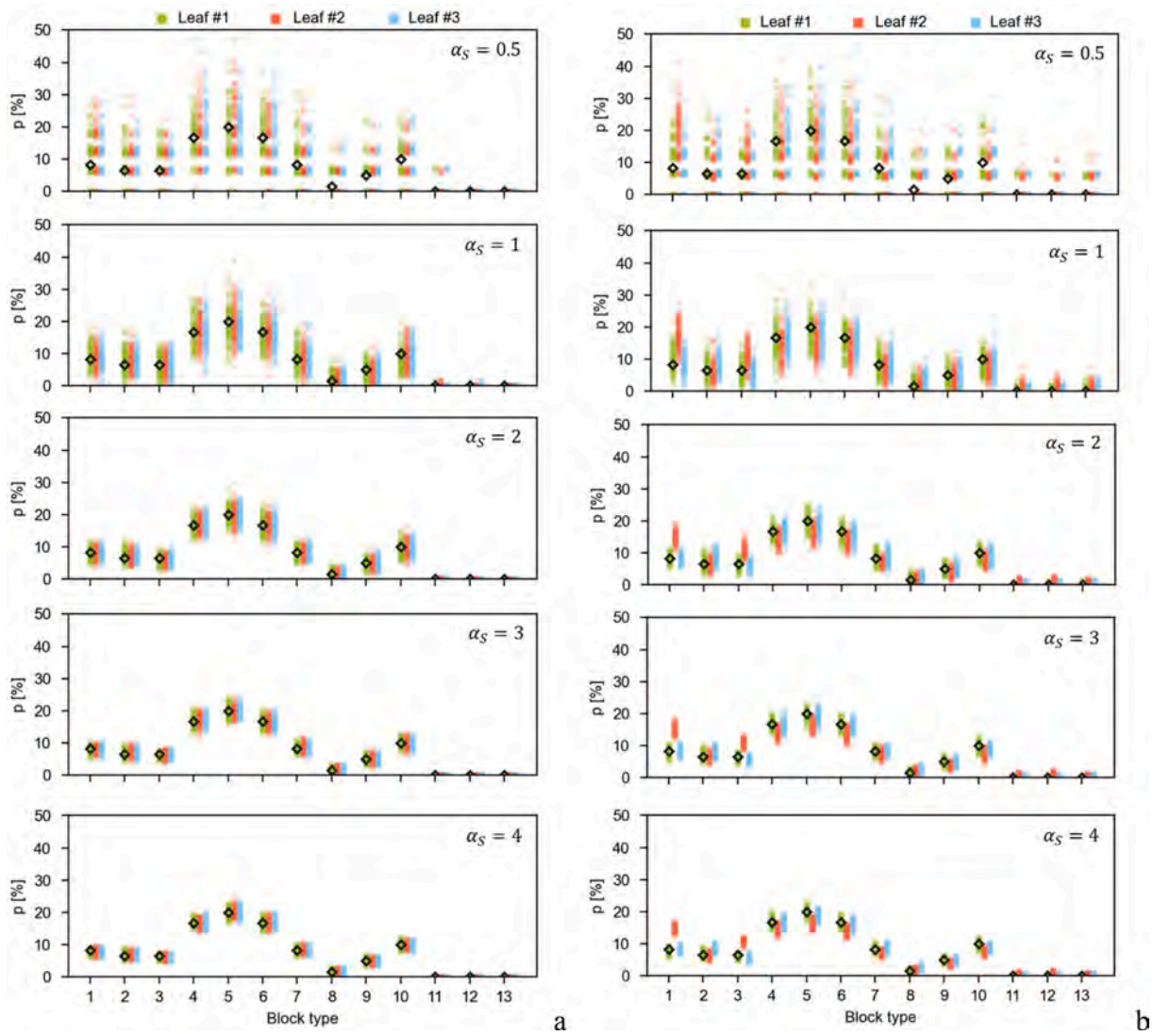**Fig. 3.** Flowchart of the volume filling process.

Fig. 4. Samples and filled volume block statistics as a function of the target-to-sample size ratio (α_s) for samples (a) without and (b) with through-thickness blocks.
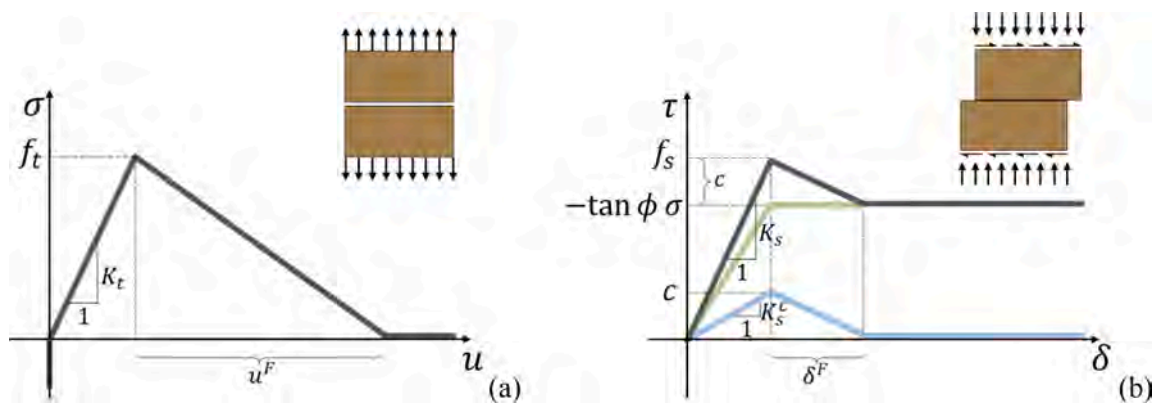

Fig. 5. Contact-based block-to-block interfaces: (a) tensile cohesive and (b) shear cohesive-frictional contact responses.

atypical in real CH structures. Because the dimensions of the available blocks may not suffice to perfectly fill the volume, and the volume filling is performed in a block-by-block basis akin to real construction phases (in contrast to global optimization approaches), in some locations an *ad hoc* block type, not present in $\mathscr{T}$, is inserted to fill any remaining gaps. Each inserted block is uniquely identified and a list $\mathscr{P}$ of the inserted

parts is kept throughout the filling process. Further, to reduce the number of *ad hoc* blocks, after a row is filled the algorithm checks if it is possible to merge an *ad hoc* block with its neighbour to produce a block that exists in $\mathscr{T}$. The procedure just described is summarized in a
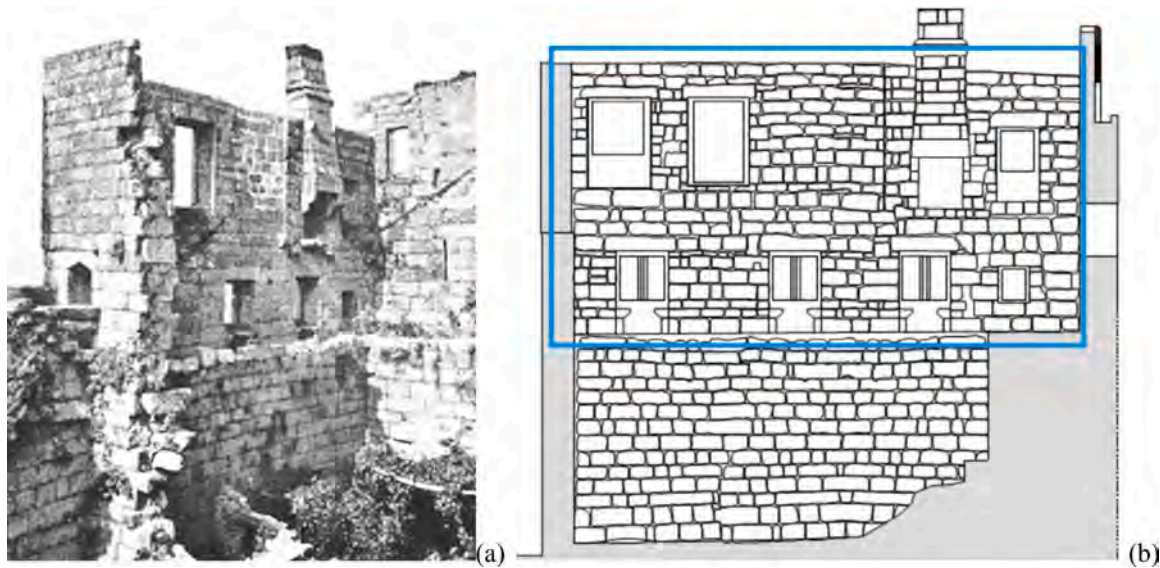
Fig. 6. Alcaçova wall of the Guimarães castle: (a) historic picture, and (b) considered portion of the structure in agreement with [35] (pictureadapted from [35]).
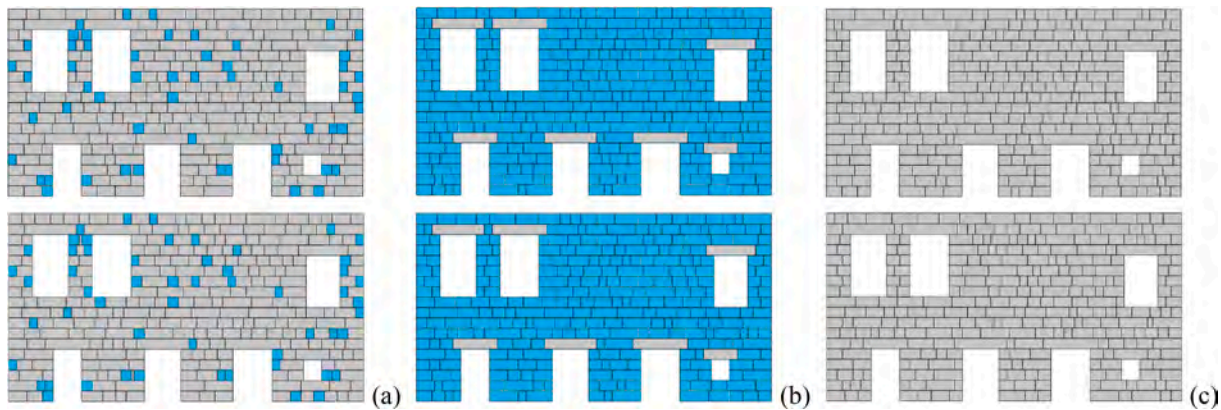

Fig. 7. Considered masonry patterns of the inner (top) and outer (bottom) leaves (through-thickness blocks are highlighted in blue): (a) Actual texture, (b) All through-thickness blocks, and (c) Not though-thickness blocks. (For interpretation of the references to color in this figure legend, the reader is referred to the web version of this article.)
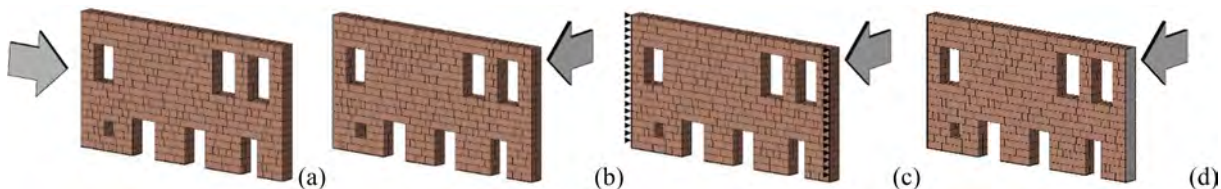

Fig. 8. Considered load scenarios: (a) in-plane loaded free-standing wall clamped at the base, (b) out-of-plane loaded free-standing wall clamped at the base, (c) out-of-plane loaded wall clamped at the base with horizontal supports on two vertical edges, (d) out-of-plane loaded wall clamped at the base and at lateral sides. Note that the arrows represent schematically the horizontal load direction.

Table 1
Mortar joint properties, in agreement with [35].

	f_t	c	ϕ
Weak mortar (WM)	0.05 MPa	0.05 MPa	30°
Strong mortar (SM)	0.30 MPa	0.30 MPa	30°

pseudocode format presented in Algorithm 1.

(*continued on next column*)

(*continued*)

Algorithm 1: Fill volume

Algorithm 1: Fill volume

Input: Target volume $\mathcal{V}$; Blocks list $\mathcal{B}$; Parts list $\mathcal{P}$; Constraints $\mathcal{C} = \{\mathcal{C}_e\}$; pmf $p[\mathcal{I}]$
Output: Filled target volume $\mathcal{V}$; Updated parts list $\mathcal{P}$
for each layer **do**
    for each leaf **do**
        $\mathcal{I} \leftarrow$ Index positions of leftmost voxel
        while row is not filled **do**
            if $\mathcal{V}[\mathcal{I}]$ is unfilled **then**
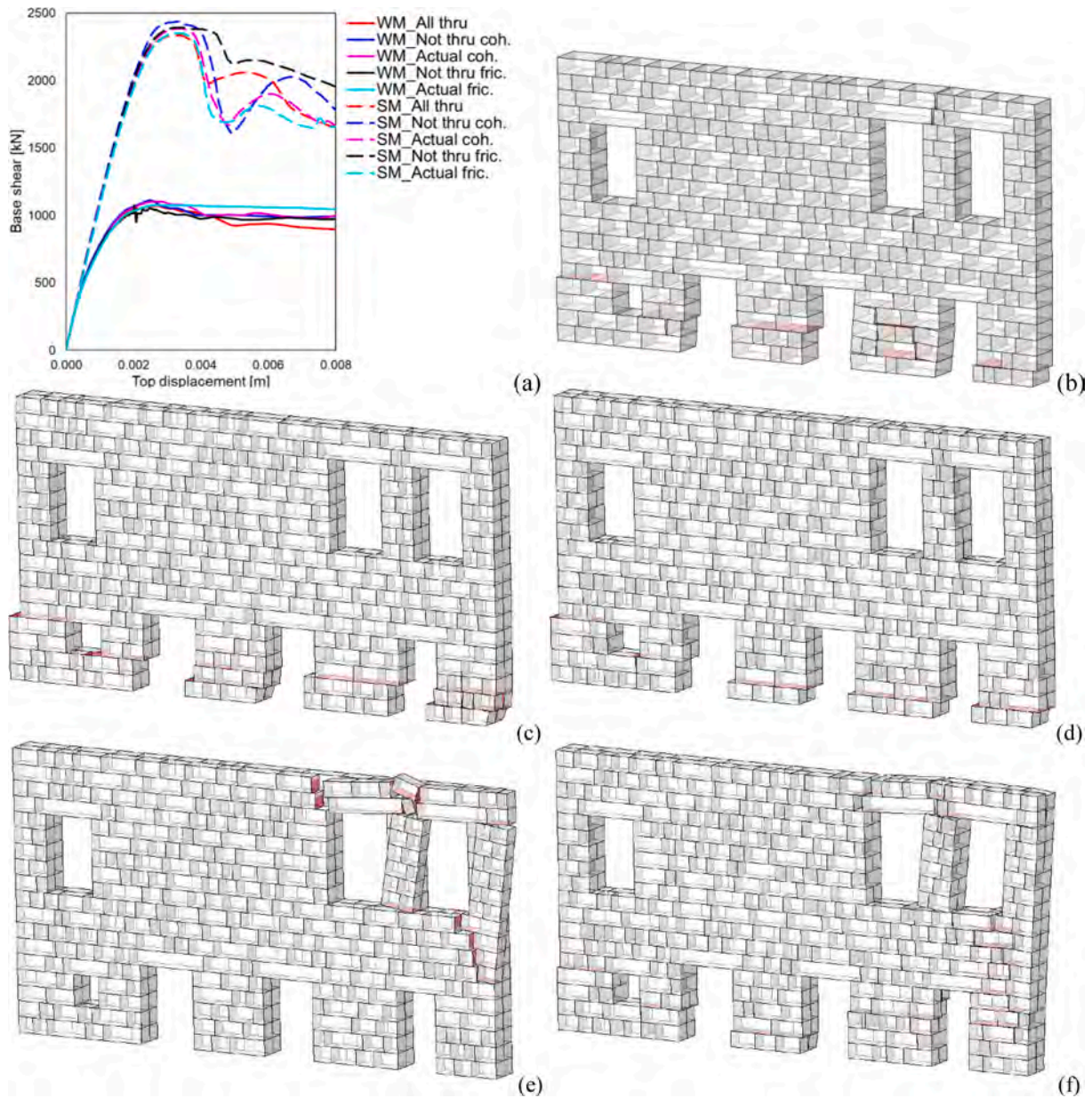
(*continued on next page*)

Fig. 9. In-plane loaded free-standing wall clamped at the base. (a) Comparison of pushover curves. Collapse mechanisms (WM cases) of: (b) all through-thickness blocks "WM_All thru", (c) not through-thickness blocks with intralayer cohesion "WM_Not thru coh.", (d) actual texture with intralayer cohesion "WM_Actual coh.", (e) not through-thickness blocks without intralayer cohesion (friction only) "WM_Not thru fric.", and (f) actual texture without intralayer cohesion (friction only) "WM_Actual fric.".

(*continued*)

Algorithm 1: Fill volume
$\mathscr{S}_{\mathscr{B}} = \{\mathscr{B}_k\}_{k=1}^{N_C} \leftarrow$ Block types respecting constraints $\mathscr{C}$ at $\mathscr{V}[\mathscr{I}]$.
if $\mathscr{S}_{\mathscr{B}} \neq \varnothing$ **then**
$b_k \leftarrow$ sampled block type using $p[\mathscr{S}_{\mathscr{B}}]$.
Generate an unique block identifier and add to $\mathscr{P}$.
Insert b_k into $\mathscr{V}[\mathscr{I}]$.
else
Generate an unique block identifier and add to $\mathscr{P}$.
Insert *ad hoc* block to fill gap at $\mathscr{V}[\mathscr{I}]$.
if $\exists$ unfilled voxel along the row **then**
$\mathscr{I} \leftarrow$ Index of next unfilled empty voxel along the row.
else
for each ad hoc block and row neighbor block pair (b_{ah}, b_n) **do**
if $b_{ah} \cup b_n \in \mathscr{B}$ **then**
Generate an unique block identifier and add to $\mathscr{P}$.
Remove b_{ah}, b_n identifiers from $\mathscr{P}$.
Merge b_{ah} and b_n.

The process described above can be used to fill up $\mathscr{V}$. However, it is common for masonry structures to have higher quality construction at corners and edges (e.g., interlocking blocks, larger blocks) for construction stability reasons, but the process just described does not differentiate inner regions from edges. To address this, the filling of the corners is performed prior to the filling of the inner regions of $\mathscr{V}$. The sampling of blocks occurs in the same manner, based on the proportions of the J as in Eqs. (1) and (2), but the filling procedure moves vertically after one block is inserted, until the edge is vertically filled. As the algorithm seeks to avoid alignment, it generates an interlocking pattern at the edges. Further, we constrain the minimum and maximum block width to be inserted into the edges, to reduce the occurrence of small blocks, when possible, based on a ratio r^* of the available filling space. We designate this latter requirement as constraint $\mathscr{C}_w$. The filling of
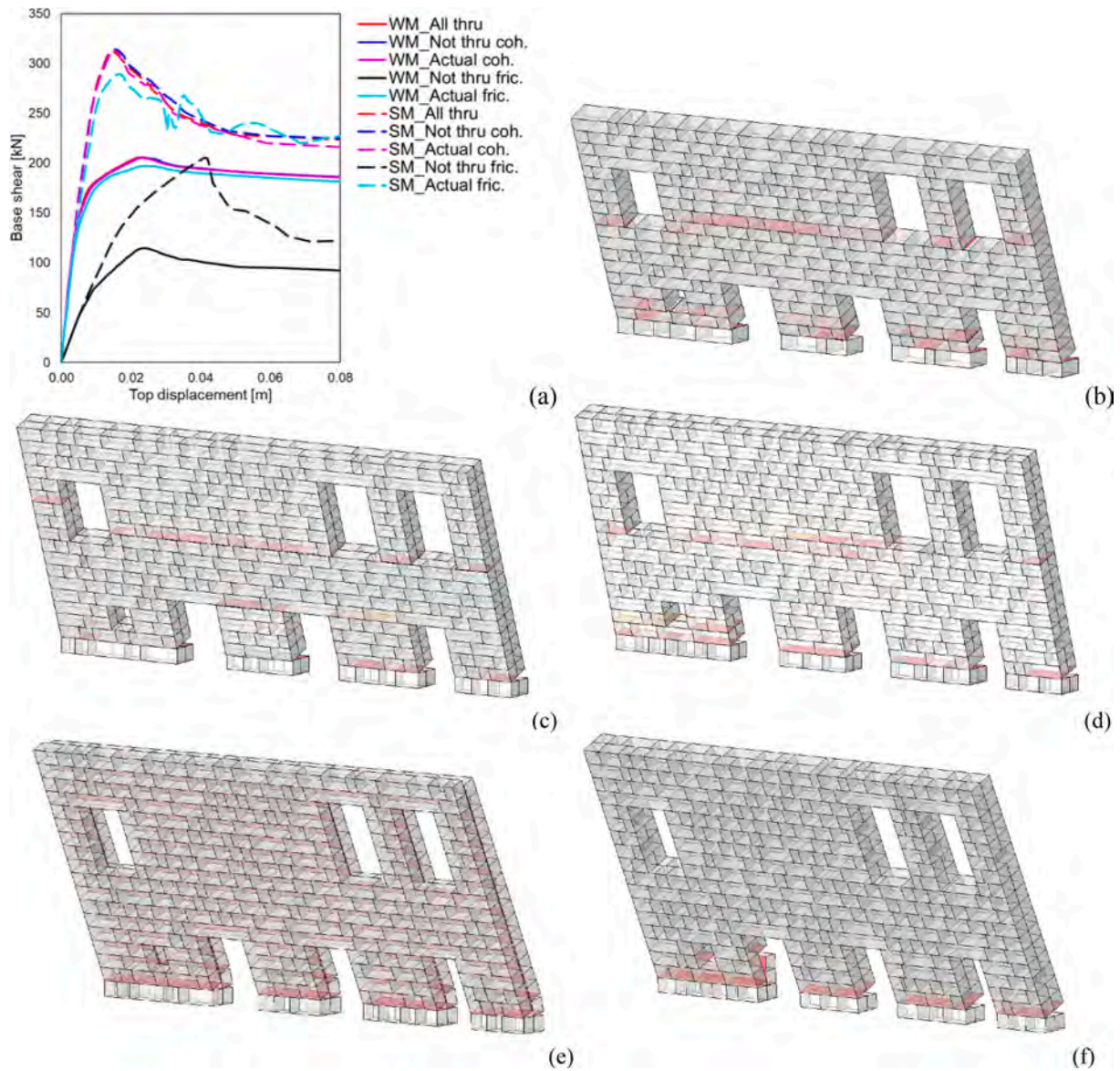
Fig. 10. Out-of-plane loaded free-standing wall clamped at the base. (a) Comparison of pushover curves. Collapse mechanisms (WM cases) of: (b) all through-thickness blocks "WM_All thru", (c) not through-thickness blocks with intralayer cohesion "WM_Not thru coh.", (d) actual texture with intralayer cohesion "WM_Actual coh.", (e) not through-thickness blocks without intralayer cohesion (friction only) "WM_Not thru fric.", and (f) actual texture without intralayer cohesion (friction only) "WM_Actual fric.".

edges is summarized in pseudocode format in Algorithm 2.

Algorithm 2: Fill corners/edges

Input: Target volume $\mathcal{V}$; Blocks list $\mathcal{B}$; Parts list $\mathcal{P}$; Constraints $\mathcal{C} = \{\mathcal{C}_e, \mathcal{C}_w\}$; pmf $p[\mathcal{S}]$

Output: Target volume with edges $\mathcal{V}$; Updated parts list $\mathcal{P}$

for each layer **do**

    for each leaf **do**

        $\{\mathcal{I}_j\}_{j=1}^{N_{edges}} \leftarrow$ Index positions of vertical edges

        for $\mathcal{I}_j \in \{\mathcal{I}_j\}_{j=1}^{N_{edges}}$ **do**

            $\{\mathcal{B}_k\}_{k=1}^{N_c} \leftarrow$ Block types respecting constraints $\mathcal{C}$ at $\mathcal{V}[\mathcal{I}_j]$.

            if $\{\mathcal{B}_k\}_k^{N_c} \neq \varnothing$ **then**

                Sample a block type.

                Generate an unique block identifier and add to $\mathcal{P}$.

                Insert block into $\mathcal{V}[\mathcal{I}_j]$.

            else

                Generate an unique block identifier and add to $\mathcal{P}$.

                Insert *ad hoc* block to fill gap.

As previously mentioned, it is possible to designate non-fillable regions, i.e., openings, in the target volume $\mathcal{V}$. Typically, such openings in a real structure require placement of a supporting lintel. Concordantly, we introduce a step that automatically identifies non-fillable regions and introduce lintels of a suitable size. In this specific study, the lintel dimensions are controlled by parameters $\mathcal{L} = (w_L^*, h_L, d_L)$, where w_L^* is the supported length of the lintel (see Fig. 2), h_L is the height of the lintel, and d_L is the depth of the lintel. The process of adding lintel is summarized as a pseudocode in Algorithm 3.

Algorithm 3: Add lintels

Input: Target volume $\mathcal{V}$; Parts list $\mathcal{P}$; Lintel parameters $\mathcal{L}$

Output: Target volume with lintels $\mathcal{V}$; Updated parts list $\mathcal{P}$

for each leaf **do**

    $\{\mathcal{I}_j\}_{j=1}^{N_{edges}} \leftarrow$ Index positions of horizontal edges

    for $\mathcal{I}_j \in \{\mathcal{I}_j\}_{j=1}^{N_{edges}}$ **do**

        Generate a unique lintel identifier and add to $\mathcal{P}$.

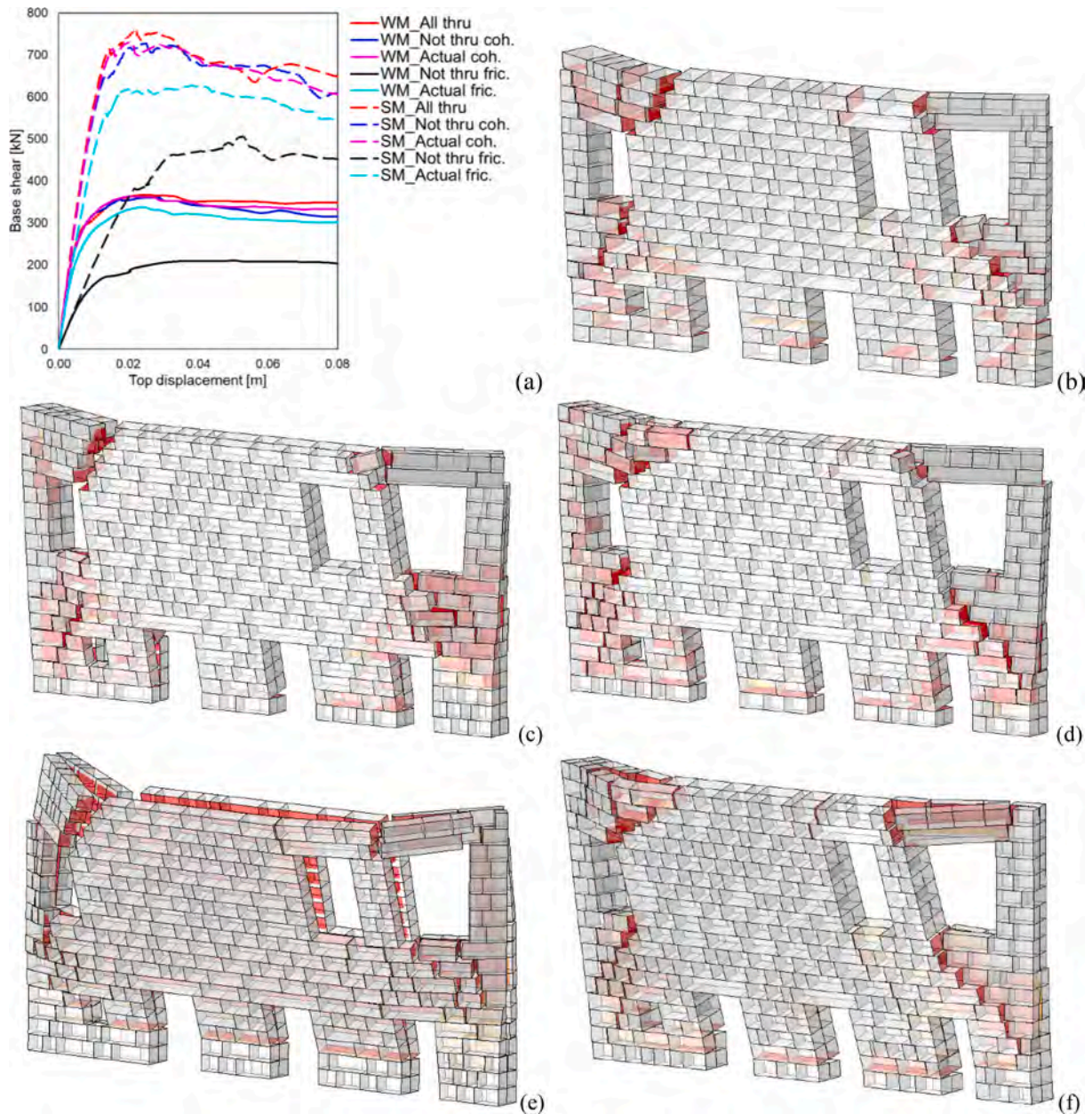   Insert lintel into $\mathcal{V}[\mathcal{I}_j]$.

Fig. 11. Out-of-plane loaded wall clamped at the base with horizontal supports on two vertical edges. (a) Comparison of pushover curves. Collapse mechanisms (WM cases) of: (b) all through-thickness blocks "WM_All thru", (c) not through-thickness blocks with intralayer cohesion "WM_Not thru coh.", (d) actual texture with intralayer cohesion "WM_Actual coh.", (e) not through-thickness blocks without intralayer cohesion (friction only) "WM_Not thru fric.", and (f) actual texture without intralayer cohesion (friction only) "WM_Actual fric.".

Thus, the overall volume filling method starts with the specification of a target volume, that in general may contain both prefilled and non-fillable regions, followed by insertion of lintels above non-fillable regions, filling of edges and corners, and finally filling of the inner regions of the volume. For each layer filled in the last stage, a follow-up adjustment step tries to minimize the number of *ad hoc* blocks by checking if a block present in $\mathcal{T}$ can be obtained by merging the *ad hoc* block with neighboring blocks. Although this operation may locally slightly alter the block statistics, it typically concerns zones close to edges and openings (where also real masonry patterns present peculiar features due to construction needs), and its effect on the overall block statistics is typically negligible. The overall procedure just described is summarized in the flowchart shown in Fig. 3.

2.2. Statistically-consistent pattern

In this section, we investigate the relationship between the sample $\mathcal{T}$ texture statistics and the filled volume $\mathcal{V}$ statistics as a function of their relative sizes. Particularly, we assess how the filled volume preserves the statistical properties of the sample, especially for multi-leaf textures, as the presence of through-thickness blocks and the requirement of non-alignment may impact the ability of the generative process to insert a new block following $p[\mathscr{B}]$. For this reason, we investigate the preservation of these statistics as a function of the ratio between the sizes of the texture sample and the target volume. The target volume size is generated by scaling the height and width of the target sample by α_S, considering a three-leaf wall of equal depth for all cases. Further, it does not contain openings to avoid artifacts in the statistics. For each scaling case, 100 samples of filled volume are generated. In Fig. 4, we show the
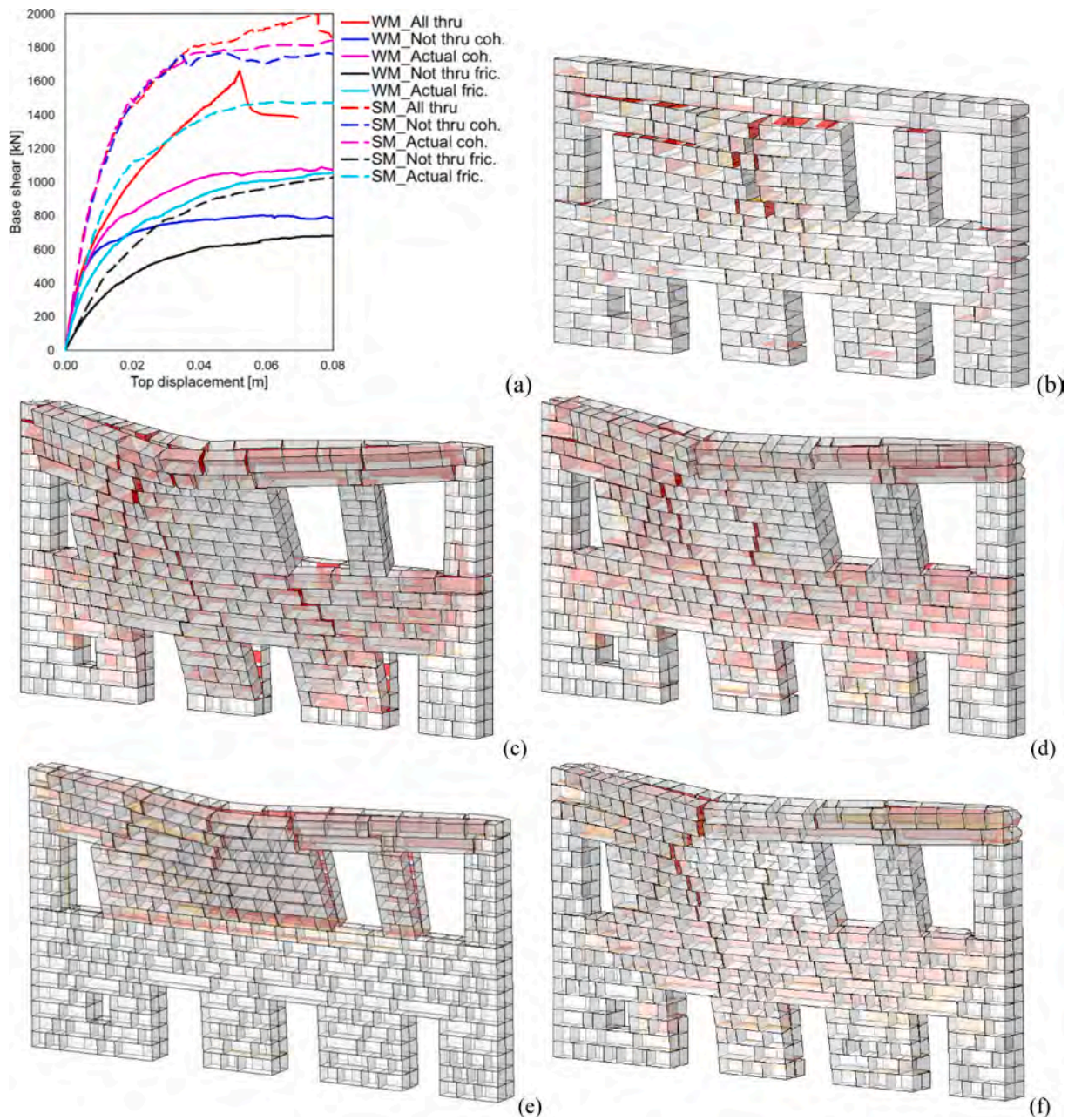
Fig. 12. Out-of-plane loaded wall clamped at the base and at lateral sides. (a) Comparison of pushover curves. Collapse mechanisms (WM cases) of: (b) all through-thickness blocks "WM_All thru", (c) not through-thickness blocks with intralayer cohesion "WM_Not thru coh.", (d) actual texture with intralayer cohesion "WM_Actual coh.", (e) not through-thickness blocks without intralayer cohesion (friction only) "WM_Not thru fric.", and (f) actual texture without intralayer cohesion (friction only) "WM_Actual fric.".

resulting block proportions for $\alpha_S = 0.5, 1, 2, 3, 4$ for samples without (Fig. 4a) and with (Fig. 4b) through-thickness blocks. The y-axis of each subfigure represents the percentage of blocks. The black and white dots correspond to the percentage of each block type on the sample, while the color-coded dots correspond to the percentage of each block on each leaf of the filled texture.

Fig. 4a suggests that if the target volume is much smaller than the sample size (see $\alpha_S = 0.5$), the dispersion in proportions is high, and *ad hoc* blocks are selected frequently. For a target volume of the same size ($\alpha_S = 1$) the block proportions are significantly closer to the target, and the proportions are sustained throughout multiple leaves. The dispersion is further reduced as α_S increases (see Fig. 4a with $\alpha_S = 2, 3, 4$).

In Fig. 4b, which concerns samples with through-thickness blocks, a similar dispersion pattern is observed with $\alpha_S = 0.5$ and $\alpha_S = 1$,

although with a higher frequency of *ad hoc* blocks. The dispersion is reduced, and *ad hoc* blocks are selected less often, proportionally, as α_S increases (see Fig. 4b with $\alpha_S = 2, 3, 4$). Notice the small deviation from target percentage (5 to 10%) of through-thickness blocks (types 1 and 3) in the second leaf. This suggests, as expected, that through-thickness blocks are the most impacted when the space is partially prefilled, and that proportions of other block types remain close to the target.

The study above indicates that the block proportions of the given sample texture are largely preserved for target volumes of at least the sample size, with increased control as the target size is increased. Then, if the sample texture is indeed representing the actual texture of the structure, the pattern generated will be consistent with the proportions observed in the real structure.

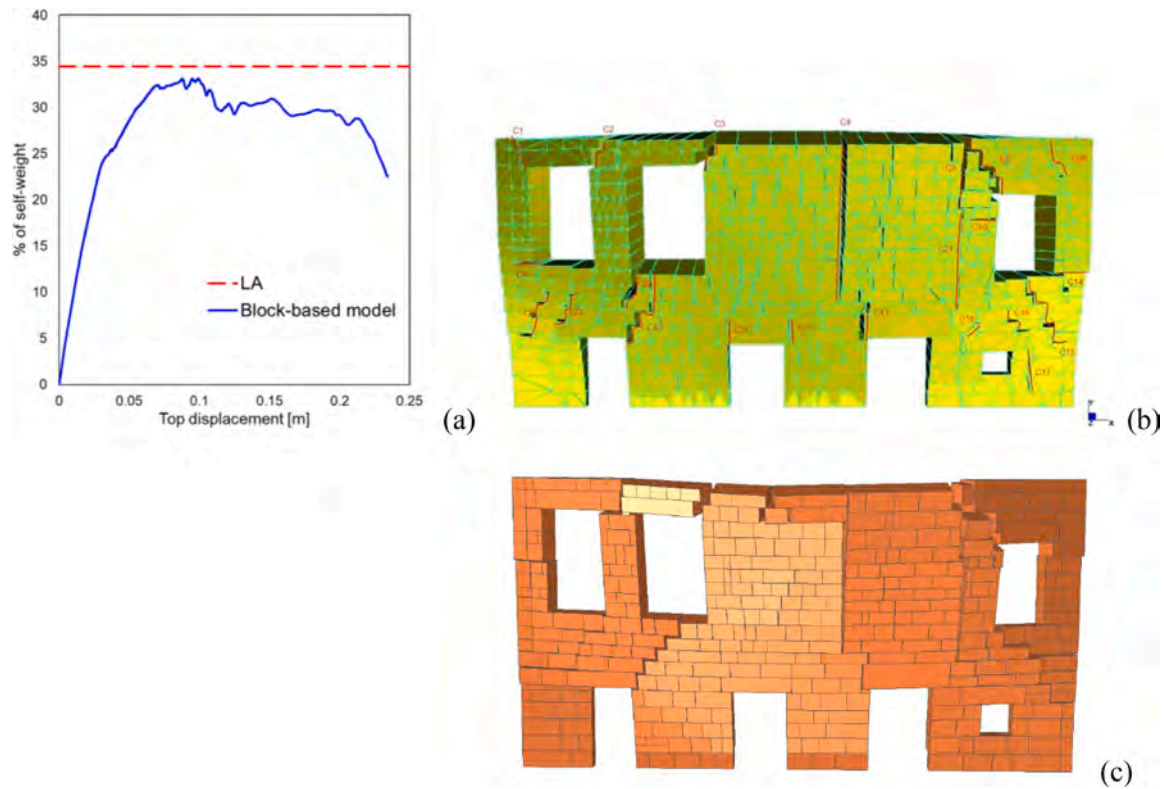It should be underlined that the voxel-based block-by-block pattern

Fig. 13. Model validation (out-of-plane loaded wall, SM case). (a) Pushover curve compared with limit analysis maximum shear. (b) Reference crack pattern from limit analysis (picture adapted from [35]). (c) Block-based model crack pattern.

Table 2
Mechanical properties of the block-based model assumed for the Alcaçova wall.

Contact mechanical properties			
Tensile behaviour		**Shear behaviour**	
f_t [MPa]	$0.05 \div 0.30$	c [MPa]	$0.05 \div 0.30$
u^F [mm]	0.5	δ^F [mm]	0.5
K_t [N/m³]	$1.0 \; 10^{10}$	K_s^c [N/m³]	$0.5 \bullet 10^{10}$
		ϕ [°]	30

Block mechanical properties			
Young's modulus [MPa]	4800		
Poisson's ratio [\]	0.17		
Density [kg/m³]	2700		

Tensile uniaxial nonlinear behaviour			Compressive uniaxial nonlinear behaviour		
Stress [MPa]	Inelastic strain	d_t [\]	Stress [MPa]	Inelastic strain	d_c [\]
1.0	0	0	12.0	0	0
0.1	0.001	0.9	12.0	0.004	0
			1.2	0.012	0.9

generator herein proposed is fully automatic. Furthermore, the generated pattern is usable, in general, by any block-based model for structural analysis, such as discrete element models [37,38,39,40,9], rigid block models [41,42,43], applied element models [44], etc. In this work, a specific routine to export the block geometries in Abaqus [45] has been developed and used.

3. Numerical modelling

3.1. Block-based modelling approach

The block-based modelling approach employed for numerical analysis, which was originally developed and validated in [3], is herein briefly recalled. The model considers nonlinear continuum blocks which interact through zero-thickness contact-based interfaces.

3.1.1. Nonlinear continuum: Block response

The nonlinear continuum behavior of blocks is assumed to be governed by the isotropic plastic-damage constitutive model developed by Lee and Fenves [46]. Such model considers two independent damage variables for tension $(0 \leq d_t < 1)$ and compression $(0 \leq d_c < 1)$. Accordingly, the uniaxial stress–strain relationships in tension and compression, respectively, are:

$$\begin{aligned} \sigma_t &= (1 - d_t) E_B (\varepsilon_t - \varepsilon_t^p), \\ \sigma_c &= (1 - d_c) E_B (\varepsilon_c - \varepsilon_c^p), \end{aligned} \tag{3}$$

where E_B is the Young's modulus of the blocks, σ_t and σ_c are the uniaxial tensile and compressive stresses, ε_t and ε_c are the uniaxial tensile and compressive strains, and ε_t^p and ε_c^p are the uniaxial tensile and compressive plastic strains. In particular, the uniaxial stress–strain curves in tension and compression represent the main input data of the continuum model. Additionally, a nonassociative flow rule is considered to account for the dilatancy and to define the plastic strain rate, whereas a multiple-hardening Drucker-Prager type surface is considered as yield surface. The interested reader is referred to [3] for further details about the setting of this constitutive law for masonry blocks.

3.1.2. Contact-based interface: Joint response

A node-to-surface contact-based cohesive-frictional formulation is assumed for the joint response (see [3] for more details). In the normal
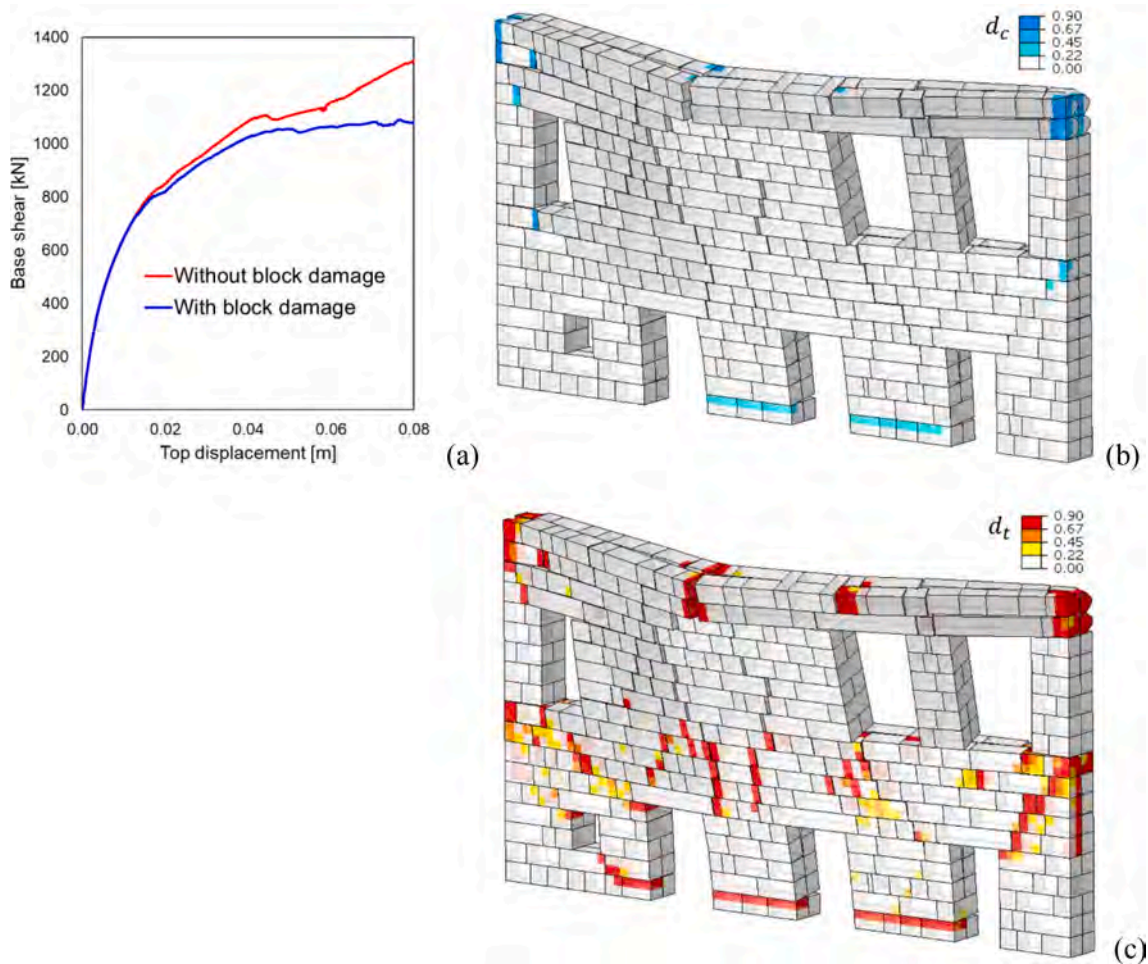
Fig. 14. Block damage influence. (a) Pushover curves comparison. (b) Compressive and (c) tensile damage contour plots for the out-of-plane loaded wall clamped at the base and at lateral sides (WM_Actual coh.).

direction, the linear relationship $\sigma = K_t u$ between the contact stress σ (positive in tension) and the normal displacement u yields in tension until the tensile strength f_t is reached (Fig. 5a), being K_t the cohesive stiffness in normal direction, while the Lagrange multiplier method is assumed to enforce the contact constraint in compression.

In the shear direction, the linear relationship $\tau = K_s \delta$ between the contact shear stress τ and the tangential slip δ between blocks, being K_s the stiffness in shear (given by both the contributions of cohesion K_s^c and friction), yields until the shear strength f_s is reached (Fig. 5b). The shear strength f_s is assumed to be function of the contact stress $f_s(\sigma) = c - \tan\phi\sigma$, where c is the shear cohesion and ϕ is the friction angle.

The maximum value of the contact stresses in the post-failure regime is described in a contact point by the relationships:

$$\sigma = (1 - D)f_t,$$
$$\tau = (1 - D)c - \tan\phi\sigma \tag{4}$$

where $0 \leq D \leq 1$ is the degradation scalar contact variable, which is assumed to vary linearly along with the displacement/slip. In Fig. 5, the quantities u^F and δ^F represent the excursion of normal displacement and slip, respectively, between the peak of cohesion ($D = 0$) and the full degradation of the contact point ($D = 1$). Finally, it should be pointed out that the frictional response is assumed to reach the regime value ($-\tan\phi\sigma$) contemporarily to the peak of shear cohesion (Fig. 5b).

3.2. Numerical set-up and load scenarios

In this section, the CH benchmark used to test the efficiency of the proposed approach, i.e., the Alcáçova wall of the Guimarães castle (Portugal), is briefly introduced (Fig. 6). The interested reader is referred to Milani et al. [35,47,48] for further details.

The so-called Alcáçova wall was originally the tallest part of a pre-existing Iberian medieval castle (Fig. 6a). Such structure is characterized by a 2-leaf (2-layer) masonry (thickness of each layer equal to 40 cm) made of granite stone ashlars with relatively regular horizontal mortar joints. The portion of the structure considered in this study, in agreement with [35], is shown in Fig. 6b.

The capability of the block-based model described in Section 3.1 to deal with full-scale structural analysis of CH structures is further assessed in Appendix A, where the results are compared with the limit analysis conducted in [35]. Indeed, Appendix A shows, beyond the adopted mechanical properties, a good agreement between the results of the present approach and the ones presented in [35].

The input data for the block-by-block pattern generation of the benchmark are shown in Fig. 1. In particular, the volume of the structure defined by $10 \times 10 \times 10$ cm voxels is shown in Fig. 1a. It should be pointed out that, in this case, the geometry has been defined adopting the dimensions and the simplifications considered in [35] (e.g. concerning the chimney, openings, and overall volume). More generally, the voxel-based volume could be automatically obtained from point clouds, for example by employing Cloud2FEM [27,28]. Furthermore, the 3D block definition of the sample in terms of $10 \times 10 \times 10$ cm voxels is shown in Fig. 1b. Such texture has been arbitrarily defined by means of 10 different block types (highlighted in Fig. 1b with different colors). Particularly, only two block types (the yellow and cyan) have been

assumed to be through-thickness blocks.

It should be pointed out that, in this case, the voxel resolutions adopted for the volume of the structure and the sample were the same (10 × 10 × 10 cm). This choice appears convenient, although is not mandatory (indeed, it is always possible to downscale/upscale the voxel resolution without changing the geometry). In general, the voxel resolutions of volume and sample should be multiples.

Three different block-by-block patterns have been generated and herein considered (Fig. 7). The first, denoted as "Actual texture" (Fig. 7a), is indeed the one generated with the sample shown in Fig. 1b, i. e., with only yellow and cyan through-thickness blocks. The second, denoted as "All through-thickness blocks" (Fig. 7b), is generated by considering all blocks of the sample in Fig. 1b as through-thickness, i.e., the wall is eventually made by one layer only. The latter, denoted as "Not though-thickness blocks" (Fig. 7c), is generated by considering none of the blocks of the sample in Fig. 1b as through-thickness, i.e., the wall is eventually made by two adjacent and distinct layers. It should be pointed out that each generated pattern has the same total thickness, which is 80 cm.

With the aim of assessing the influence of through-thickness blocks and intralayer properties (i.e., the mechanical properties of the interface between adjacent blocks from different layers) on the full-scale structural response [49], five different configurations have been considered:

- *All thru*: all through-thickness blocks;
- *Not thru coh.*: not through-thickness blocks with intralayer cohesion;
- *Actual coh.*: actual texture with intralayer cohesion;
- *Not thru fric.*: not through-thickness blocks without intralayer cohesion (friction only);
- *Actual fric.*: actual texture without intralayer cohesion (friction only).

Basically, "without intralayer cohesion (friction only)" means that cohesion is neglected in the intralayer properties and only friction is considered. This condition aims at mimicking the mechanical response of *a sacco* masonries, which are widely present in CH structures. In particular, *a sacco* masonry is characterized by intralayer gaps filled by scrap materials [50,9,51].

Four load scenarios have been considered for each configuration, employing both in- and out-of-plane nonlinear static analyses (Fig. 8):

(a) In-plane loaded free-standing wall clamped at the base (Fig. 8a);
(b) Out-of-plane loaded free-standing wall clamped at the base (Fig. 8b);
(c) Out-of-plane loaded wall clamped at the base with horizontal supports on two vertical edges (as shown in Fig. 8c);
(d) Out-of-plane loaded wall clamped at the base and at lateral sides (as shown in Fig. 8d).

In particular, the load scenarios (b), (c), and (d) can be seen as extreme cases to model the constraint offered by orthogonal walls.

Finally, for each configuration and for each load scenario, two different set-ups of mortar joints properties, namely *weak mortar* (WM) and *strong mortar* (SM), have been considered, see Table 1, in agreement with [35].

Each nonlinear pushover-like analysis is characterized by two steps. In the first step, a gravity load is applied to each block of the structure. In the second step, a mass-proportional horizontal load is applied to the structure (through a body force on each FE) by employing a quasi-static dynamic implicit algorithm, which demonstrated to be more efficient with respect to more common arc length procedures [3].

4. Results and discussion

In this section, the results of the 40 nonlinear static analyses previously listed are presented and discussed. It should be pointed out that the structural analyses herein performed are not intended to be used for

structural assessment of the CH structure (Alcaçova wall), but rather the CH structure is used as a benchmark to assess the influence of through-thickness blocks and intralayer properties on the full-scale structural response, highlighting thus the potentialities of the block pattern generator.

The results of the four load scenarios are shown in Figs. 9–12 in terms of pushover curves (base shear – top displacement) and collapse mechanisms. It should be pointed out that the computation of the base shear for load scenarios (c) and (d) considered the horizontal reactions of the constrained nodes on the lateral sides as well. For the sake of brevity, only the collapse mechanisms obtained with WM are shown. In Figs. 9–12, red color denotes fully degraded contact-based interfaces, while orange color denotes ongoing degradation in the interfaces.

Concerning the in-plane loaded wall (Fig. 9), very similar values of peak shear load (and similar pushover curves in general) can be observed between the configurations (Fig. 9a). Typically, the collapse mechanisms are characterized by a sliding in the lower portion of the structure, with the exemption of the cases in which the intralayer cohesion is not considered (Fig. 9e,f), where an overturning mechanism is observed in a top corner of the structure. Basically, the through-thickness pattern and intralayer properties do not significantly influence the force–displacement response of the structure, while they can lead to significantly different collapse mechanisms.

Concerning the out-of-plane loaded free-standing wall clamped at the base (Fig. 10), very similar pushover curves and collapse mechanisms (simple overturning) are observed within the configurations. The only exception is shown by the configuration *Not thru fric.*, which highlights the overall sliding between the two leaves. This happens together with a significantly lower peak load and stiffness with respect to the other cases, for both SM and WM cases. Interestingly, the presence of few through-thickness blocks in the *Actual fric.* configuration prevents the overall sliding between the two leaves, leading to results quasi-identical to the *All thru* configuration (even though the absence of intralayer cohesion).

Analogously to the out-of-plane loaded free-standing wall clamped at the base, also the case with horizontal supports on two vertical edges (Fig. 11) shows a significant difference between the *Not thru fric.* configuration and the others. Indeed, a complete detachment between the leaves in the central part of the structure is observed in *Not thru fric.*, while in the other cases they remain joint. This phenomenon is also observed in the pushover curve, characterized by lower peak load and stiffness with respect to the other cases, for both SM and WM cases. Also in this case, the presence of few through-thickness blocks in the *Actual fric.* configuration prevents this detachment between the two leaves, keeping the base shear very close, although slightly lower, to the *All thru* configuration.

Concerning the out-of-plane loaded wall clamped at the base and at lateral sides (Fig. 12), the results are more scattered than the other load scenarios. Also in this case, the *Not thru fric.* configuration shows the lowest stiffness and peak shear load. The collapse mechanism is characterized by the overturning of the upper central part of the wall, where the two leaves are completely detached (Fig. 12e). As before, the presence of few through-thickness blocks in the *Actual fric.* configuration leads to a more global mechanism, characterized by a pseudo-vertical crack around the wall center (Fig. 12f). This mechanism is characterized by higher stiffness and shear capacity with respect to the *Not thru fric.* one. Conversely, the *Not thru coh.* configuration, which has a higher initial stiffness with respect to the two aforementioned cases, shows a complete detachment between the leaves in the wall lower portion, and shows a peak base shear lower than the *Actual fric.* one (WM case). This trend is not observed in the SM case, where *Not thru coh.* does not show any leaves detachment, resulting rather similar to the *All thru* and *Actual coh.* cases in terms of pushover curves. Finally, it should be pointed out that transversal compression arises in this load scenario, given the confinement exerted by clamped sides. This eventually leads to compressive damage in some blocks of the wall, as shown e.g. in

Appendix B together with the influence of block nonlinearity on the structural response. Additionally, blocks located in the clamped sides eventually show tensile damage due to flexure.

The generalization of the outcomes herein discussed should be carefully considered, as collapse mechanisms may differ due to different block-by-block patterns, block mechanical properties, external loads, boundary conditions, etc. However, the importance of keeping track of the main features of the masonry pattern in full-scale structural analyses is herein highlighted.

5. Conclusions

In this paper, an automatic block-by-block pattern generator based on voxels has been developed for multi-leaf nonperiodic masonries. The outcomes of this algorithm have been then directly employed in full-scale block-based computational analysis of historical masonry structures.

Such generator has been based on two main input data. The first one is the 3D volume of the structure in terms of voxels, which has been proven to be directly obtainable from point clouds [27,28]. The second is the 3D block definition in a sample, also given in terms of voxels. Then, the voxel volume is automatically filled with blocks by keeping the blocks statistics of the sample, as well as accounting for through-thickness blocks and structural details, such as lintels and edges.

A CH benchmark (Alcaçova wall of the Guimarães castle [35]) has been adopted to assess the efficiency of the filling algorithm. Also, the capability of the algorithm to generate statistically-consistent patterns has been verified. Thus, such benchmark has been employed in full-scale in-plane and out-of-plane computational analyses by using the damaging block-based model previously developed in [3]. Various multi-leaf patterns, with different indexes of through-thickness blocks, have been considered and critically compared in structural analysis, highlighting the influence of through-thickness blocks and intralayer mechanical properties on the overall structural response.

As main result, the presence of few through-thickness blocks appears to significantly increase the out-of-plane capacity when intralayer cohesion is not considered. This outcome may be particularly appealing when dealing with *a sacco* masonry, characterized by quasi-zero intra-layer cohesion. In detail, the presence of few through-thickness blocks prevents the overall sliding/detaching between adjacent leaves, enhancing the mechanical capacity of the structure. In any case, the generalization of these outcomes should be carefully considered. Indeed, the structural response may differ due to different block-by-block patterns, block mechanical properties, external loads, boundary conditions, etc. Nonetheless, the importance of keeping track of the main features of the masonry pattern in full-scale structural analyses has been herein highlighted quantitatively.

Finally, the choice of adopting voxels in the filling algorithm appeared particularly appealing, as it always guarantees the achievement of volume filling with blocks, without introducing geometrical issues. Future developments will concern the extension of the algorithm to orthogonal walls (possibly by implementing a change of coordinates and, in the corners, the alternation of blocks belonging to the different orthogonal walls) and irregular stone masonry types, that could still employ voxels (possibly with a finer voxel resolution and a subsequent block smoothing).

CRediT authorship contribution statement

M. Pereira: Data curation, Formal analysis, Methodology, Software, Validation, Writing – original draft, Writing – review & editing. **A.M. D'Altri:** Conceptualization, Data curation, Funding acquisition, Methodology, Software, Validation, Writing – original draft, Writing – review & editing. **S. de Miranda:** Funding acquisition, Methodology, Supervision, Writing – review & editing. **B. Glisic:** Funding acquisition, Methodology, Supervision, Writing – review & editing.

Declaration of Competing Interest

The authors declare that they have no known competing financial interests or personal relationships that could have appeared to influence the work reported in this paper.

Data availability

Data are attached in the Supplementary Material section.

Appendix A

In this appendix, the out-of-plane analysis results on the Alcaçova wall obtained with the damaging block-based model [3] are compared with the ones obtained with the block-based limit analysis in [35], see Fig. 13. For the sake of comparison, the simplifications and boundary conditions adopted in [35] have been also considered here.

In particular, a single masonry layer (thickness 40 cm) has been considered as in [35], by implementing the very same block-by-block pattern adopted in [35] (generated manually from the geometry shown in [35]). Also, the boundary conditions have been assumed to mimic the ones adopted in [35], i.e., the out-of-plane loaded wall is supported on three edges (lower and two vertical edges). Particularly, horizontal supports with axis parallel to the out-of-plane direction have been considered at mid-thickness of the wall in the two vertical edges. This hypothesis has been made to bring the assumptions in the present approach closer to the ones considered in [35], where plate elements have been adopted.

The mechanical properties of the block-based model assumed for the Alcaçova wall (granite blocks) are shown in Table 2, assumed in agreement with [35] where possible. Other general parameters of the continuum constitutive law have been assumed as in [3]. The blocks have been meshed with 8-node hexahedral finite elements, with a mesh seed equal to 10 cm.

The comparison of the results is shown in Fig. 13, in terms of comparison of the pushover curve with limit analysis maximum shear (Fig. 13a) and crack pattern between limit analysis (Fig. 13b) and damaging block-based model (Fig. 13c) collapse mechanisms. As it can be noted, the maximum base shear (in terms of percentage of self-weight) is rather similar between the two models, as well as the collapse mechanism composed of a combination of pseudo-vertical cracks in the wall central part and diagonal cracks between the openings.

Accordingly, the damaging block-based model appears able to reproduce literature results on out-of-plane loaded structures with nonperiodic block-by-block masonry patterns.

Appendix B

In this appendix, the influence of block nonlinearity on the structural response of the CH benchmark is shown (Fig. 14). In particular, the pushover curves with and without block damage of the out-of-plane loaded wall clamped at the base and at lateral sides (WM_Actual coh.) are shown and compared in Fig. 14a. As it can be noted, the case without

block damage is characterized by a significant hardening which leads to an overestimation of the lateral capacity of the structure. In the case with block damage, crushing is observed in the blocks in the top lateral corners, in the top central part, and in the compressed toe of the two central piers at the bottom of the structure (Fig. 14b). Tensile damage (Fig. 14c) is instead more widespread over the structure, with a concentration on the top corners where blocks underwent flexure.

Appendix C. Supplementary material

Supplementary data to this article can be found online at https://doi.org/10.1016/j.engstruct.2023.115945.

References

[1] D'Altri A, Sarhosis V, Milani G, Rots J, Cattari S, Lagomarsino S, et al. Modeling strategies for the computational analysis of unreinforced masonry structures: Review and classification. Arch Comput Meth Eng 2020;27:1153–85.

[2] Beatini V, Royer-Carfagni G, Tasora A. A non-smooth-contact-dynamics analysis of Brunelleschi's cupola: an octagonal vault or a circular dome? Meccanica 2019;54 (3):525–47.

[3] D'Altri AM, Messali F, Rots J, Castellazzi G, de Miranda S. A damaging block-based model for the analysis of the cyclic behaviour of full-scale masonry structures. Eng Fract Mech 2019;209:423–48.

[4] Ferrante A, Clementi F, Milani G. Advanced numerical analyses by the Non-Smooth Contact Dynamics method of an ancient masonry bell tower. Math Methods Appl Sci 2020;43(13):7706–25.

[5] Ferrante A, Loverdos D, Clementi F, Milani G, Formisano A, Lenci S, et al. Discontinuous approaches for nonlinear dynamic analyses of an ancient masonry tower. Eng Struct 2021;231:111626.

[6] Ferrante A, Schiavoni M, Bianconi F, Milani G, Clementi F. Influence of stereotomy on discrete approaches applied to an ancient church in Muccia, Italy. J Eng Mech 2021;147(11):04021103.

[7] Malena M, Portioli F, Gagliardo R, Tomaselli G, Cascini L, de Felice G. Collapse mechanism analysis of historic masonry structures subjected to lateral loads: a comparison between continuous and discrete models. Comput Struct 2019;220: 14–31.

[8] de Felice G, Fugger R, Gobbin F. Overturning of the façade in single-nave churches under seismic loading. Bull Earthq Eng 2021;20:941–962.

[9] Pulatsu B, Bretas EM, Lourenco PB. Discrete element modeling of masonry structures: validation and application. Earthq Struct 2016;11(4):563.

[10] Ferrante A, Giordano E, Clementi F, Milani G, Formisano A. FE vs. DE modeling for the nonlinear dynamics of a historic church in central Italy. Geosciences 11(5); 2021:189.

[11] Casolo S, Milani G. Simplified out-of-plane modelling of three-leaf masonry walls accounting for the material texture. Constr Build Mater 2013;40:330–51.

[12] Cavalagli N, Cluni F, Gusella V. Evaluation of a statistically equivalent periodic unit cell for a quasi-periodic masonry. Int J Solids Struct 2013;50(25–26):4226–40.

[13] Binda L, Pina-Henriques J, Anzani A, Fontana A, Lourenço PB. A contribution for the understanding of load-transfer mechanisms in multi-leaf masonry walls: testing and modelling. Eng Struct 2006;28(8):1132–48.

[14] Milani G. 3D upper bound limit analysis of multi-leaf masonry walls. Int J Mech Sci 2008;50(4):817–36.

[15] Tiberti S, Milani G. 3D homogenized limit analysis of non-periodic multi-leaf masonry walls. Comput Struct 2020;234:106253.

[16] Boscato G, Baraldi D, de Carvalho Bello CB, Cecchi A. Interface modeling in load transfer mechanisms of multi-leaf masonry panels. Eng Struct 2022;266:114633.

[17] Boscato G, de Carvalho Bello CB, Cecchi A. Multi-leaf masonry walls: Load transfer mechanisms sensitivity to mechanic and geometric parameters. Structures 2021; 31:540–557.

[18] Drougkas A, Sarhosis V. Micro-mechanical homogenisation of three-leaf masonry walls under compression. Eng Struct 2021;245:112890.

[19] de Carvalho Bello CB, Boscato G, Meroi E, Cecchi A. Non-linear continuous model for three leaf masonry walls. Constr Build Mater 2020;244:118356.

[20] Szabó S, Funari MF, Lourenço PB. Masonry patterns' influence on the damage assessment of URM walls: current and future trends. Dev Built Environ 2023: 100119.

[21] Loverdos D, Sarhosis V. Automatic image-based brick segmentation and crack detection of masonry walls using machine learning. Autom Constr 2022;140: 104389.

[22] Dais D, Bal IE, Smyrou E, Sarhosis V. Automatic crack classification and segmentation on masonry surfaces using convolutional neural networks and transfer learning. Autom Constr 2021;125:103606.

[23] Loverdos D, Sarhosis V, Adamopoulos E, Drougkas A. An innovative image processing-based framework for the numerical modelling of cracked masonry structures. Autom Constr 2021;125:103633.

[24] Valero E, Bosché F, Forster A. Automatic segmentation of 3D point clouds of rubble masonry walls, and its application to building surveying, repair and maintenance. Autom Constr 2018;96:29–39.

[25] Zhang S, Hofmann M, Beyer K. A 2D typology generator for historical masonry elements. Constr Build Mater 2018;184:440–53.

[26] Shaqfa M, Beyer K. A virtual microstructure generator for 3D stone masonry walls. Eur J Mech-A/Solids; 2022:104656.

[27] Castellazzi G, D'Altri AM, de Miranda S, Ubertini F. An innovative numerical modeling strategy for the structural analysis of historical monumental buildings. Eng Struct 2017;132:229–48. https://doi.org/10.1016/j.engstruct.2016.11.032.

[28] Castellazzi G, Lo Presti N, D'Altri A, de Miranda S. Cloud2FEM: a finite element mesh generator based on point clouds of existing/historical structures. Software X; 2022.

[29] Ibrahim Y, Nagy B, Benedek C. Deep learning-based masonry wall image analysis. Remote Sens (Basel) 2020;12(23):3918.

[30] Dang LM, Wang H, Li Y, Nguyen LQ, Nguyen TN, Song HK, et al. Deep learning-based masonry crack segmentation and real-life crack length measurement. Constr Build Mater 2022;359:129438.

[31] Negri S, Aiello MA. High-resolution GPR survey for masonry wall diagnostics. J Build Eng 2021;33:101817.

[32] Lombardi F, Lualdi M, Garavaglia E. Masonry texture reconstruction for building seismic assessment: practical evaluation and potentials of ground penetrating radar methodology. Constr Build Mater 2021;299:124189.

[33] Cavalagli N, Cluni F, Gusella V. Failure surface of quasi-periodic masonry by means of statistically equivalent periodic unit cell approach. Meccanica 2018;53(7): 1719–36.

[34] Milani G, Bertolesi E. Quasi-analytical homogenization approach for the non-linear analysis of in-plane loaded masonry panels. Constr Build Mater 2017;143:723–43.

[35] Milani G, Esquivel YW, Lourenço PB, Riveiro B, Oliveira DV. Characterization of the response of quasi-periodic masonry: Geometrical investigation, homogenization and application to the Guimarães castle, Portugal. Eng Struct 2013;56:621–41.

[36] Tiberti S, Milani G. 3D voxel homogenized limit analysis of single-leaf non-periodic masonry. Comput Struct 2020;229:106186.

[37] Sarhosis V, Lemos JV, Bagi K. Discrete element modelling. In: Numerical modeling of masonry and historical structures, Woodhead Publishing Series in Civil and Structural Engineering; 2019. p. 469–501.

[38] Malomo D, DeJong MJ, Penna A. Distinct element modelling of the in-plane cyclic response of URM walls subjected to shear-compression. Earthq Eng Struct Dyn 2019;48(12):1322–44.

[39] Sarhosis V, Milani G, Formisano A, Fabbrocino F. Evaluation of different approaches for the estimation of the seismic vulnerability of masonry towers. Bull Earthq Eng 2017;16(3):1511–45.

[40] Sarhosis V, Bagi K, Lemos J, Milani G. Computational modeling of masonry structures using the discrete element method. USA: IGI Global; 2016.

[41] Gagliardo R, Portioli F, Cascini L, Landolfo R, Lourenço PB. A rigid block model with no-tension elastic contacts for displacement-based assessment of historic masonry structures subjected to settlements. Eng Struct 2021;229:111609.

[42] Cascini L, Brando G, Portioli F, Forgione MR, Mazzanti C, Vasta M. Force-based seismic evaluation of retrofitting interventions of historic masonry castles by 3D rigid block limit analysis. Appl Sci 2020;10(15):5035.

[43] Cascini L, Gagliardo R, Portioli F. LiABlock_3D: a software tool for collapse mechanism analysis of historic masonry structures. Int J Architect Herit 2018. https://doi.org/10.1080/15583058.2018.1509155.

[44] Malomo D, Pinho R, Penna A. Using the applied element method for modelling calcium silicate brick masonry subjected to in-plane cyclic loading. Earthq Eng Struct Dyn 2018;47(7):1610–30.

[45] Abaqus®. Theory manual, Version 6.22; 2022.

[46] Lee J, Fenves GL. Plastic-damage model for cyclic loading of concrete structures. J Eng Mech 1998;124(8):892–900.

[47] Riveiro B, Lourenço PB, Oliveira DV, González-Jorge H, Arias P. Automatic morphologic analysis of quasi-periodic masonry walls from LiDAR. Comput Aided Civ Inf Eng 2015;31(4):305–19.

[48] Cabaleiro M, Branco JM, Sousa HS, Conde B. First results on the combination of laser scanner and drilling resistance tests for the assessment of the geometrical condition of irregular cross-sections of timber beams. Mater Struct 2018;51(4): 1–15.

[49] Misir IS, Yucel G, Kuran F, Eser CB, Aldemir O, Topcu S. Experimental out-of-plane damage limits of historical stone masonry walls. Constr Build Mater 2022;333: 127098.

[50] Como M. Statics of Historic Masonry Constructions, Springer Series in Solid and Structural Mechanics; 2013.

[51] Napolitano R, Glisic B. Understanding the function of bonding courses in masonry construction: an investigation with mixed numerical methods. J Cult Herit 2019; 39:120–9.